



**Control of high-order harmonic emission in solids via the tailored intraband current**Tao-Yuan Du \**School of Mathematics and Physics, China University of Geosciences, Wuhan 430074, China* (Received 5 September 2021; accepted 29 November 2021; published 10 December 2021)

Delocalized Bloch electrons in solids are usually regarded as a kind of representative quantum Fermi gas. To unravel the real-space dynamics of Bloch electrons under a tailoring intraband current, we introduced a quasiparticle picture of a wave packet via superposing the multiple Bloch states within a given crystal-momentum region. We find that temporal characteristics and yield modulation in solid-state high-harmonic generation (HHG) depend sensitively on the crystal-momentum region of generating electron-hole pair. Its mechanism could be clarified by the gradual symmetrization of the time-dependent carrier distribution with the growing tunneling-momentum range. Manipulation of tunneling-momentum range is experimentally feasible via photon-carrier doping of appropriate preexcitation pulse. Finally, we elucidate the role of dephasing in the process of HHG. The scheme of customizing intraband current provides an alternative way to regulate the high-harmonic generation of solids.

DOI: [10.1103/PhysRevA.104.063110](https://doi.org/10.1103/PhysRevA.104.063110)**I. INTRODUCTION**

High-harmonic generation (HHG) from atoms and molecules is a well-known scheme for generating photon sources from the extreme ultraviolet to the soft x-ray spectral range [1–4]. High-harmonic spectroscopy has also achieved great success in probing electronic structure and dynamics in atomic and molecular systems. HHG is recently extended to solid-state ZnO material by Ghimire *et al.*, who inspires the intensive study of high-harmonic generation from a solid [5–10]. Theoretically, two types of HHG processes in solids have been identified: intraband and interband [11, 12]. For the intraband process, the harmonic radiations are derived from intraband transport or the laser-driven wave-packet oscillation within the nonlinear band dispersion. For the interband process, the generated mechanism of HHG involves recombination between the accelerated electron and hole wave packets, similar to the picture of HHG from atomic and molecular systems [12–17]. Discussions about the intraband and interband processes are based on the field-free band structure of system. Floquet-Bloch theory provides an avenue to assess the field-induced modification of energy bands (Floquet-Bloch shifts) [18–20] and the its role in HHG from solids [19–22].

In both intraband and interband processes, the first step is the electronic multiphoton or tunneling excitation, which generates the electron-hole pair. So far, in both cases, the electron-hole pairs are created around the minimal band gap or within the full region of the Brillouin zone (BZ), are adopted as the choice of initial states in the theoretical simulations of solid-state HHG [17, 23–26]. One further sees that the case within the full BZ region leads to an artificial spectroscopic dip in the below-gap range of HHG spectra, which was never observed in experiments and totally neglected in these

theoretical works as far as we know [24–29]. The crystal-momentum range determines the spatial localization (i.e., wave-particle duality) of the superposed quasiparticle wave packet and reflects the feature of intraband current within the BZ. Thus, the intraband transport and the temporal characteristic of interband emissions would be influenced by the tunneling-momentum region of generating electron-hole pairs. Actually, the tunneling-momentum region involved in solid-state HHG can be controlled by photon-carrier doping experimentally [30, 31]. The duality of the electronic wave packet is rather pervasive in the understanding of the strong-field process. The physical reality in strong-field excitation had been described successfully with different levels of wave-particle approximation [32, 33]. Furthermore, the wave-particle duality of the Bloch electronic gas in solids provides an alternative insight to distinguish the HHG mechanisms of open- and closed-trajectory models [23, 29].

In this paper we theoretically study the role of various tunneling-momentum regions in the HHG from solids and discuss their temporal features of electron-hole recombination dynamics. In addition, we clarify the emergence of the artificial spectroscopic dip within the below-gap harmonics and the variation of HHG yields as a function of range of tunneling momentum. This paper is organized as follows. In Sec. II, we present the numerical method of our simulations and describe quasiclassical motion of the time-dependent quantum wave packet. In Sec. III, we systematically investigate the HHG spectra and their yield modulations under the different tunneling-momentum regions and uncover their physical origin. We summarize our paper in Sec. IV. Atomic units are used throughout this paper, unless specified otherwise.

**II. THEORETICAL METHODS****A. Time-dependent Schrödinger equation**

Following the single active electron approximation and velocity-gauge treatment, the time-dependent Schrödinger

\*duty710@163.com

equation can be written as

$$i \frac{\partial}{\partial t} |\psi_{k_0}(t)\rangle = \left\{ \frac{[\hat{p} + A(t)]^2}{2} + V(x) \right\} |\psi_{k_0}(t)\rangle. \quad (1)$$

The periodic potential of the ZnO model along the specifically polarized direction is adopted here, and its specified form is  $V(x) = -V_0[1 + \cos(\frac{2\pi}{a_0}x)]$  with  $V_0 = 0.37$  a.u. and lattice constant  $a_0 = 8$  a.u. [34]. Under the dipole approximation,  $A(t) = -\int_{-\infty}^t F(t')dt'$  is the vector potential, and  $F(t)$  is the electric field of laser pulses with a  $\cos^2$  envelope. The wavelength and duration of the mid-infrared (MIR) laser pulses are  $2.0 \mu\text{m}$  and six optical cycles, respectively. The time grid adopts  $0.27$  a.u. ( $\approx 6.5$  as). The amplitude of the laser vector potential adopted in following simulations is  $0.3\pi/a_0$ .

The systematic eigenstate  $|\psi_k^n\rangle$  and eigenenergy  $\epsilon_n(k)$  with band index  $n$  can be obtained from the diagonalization of the field-free Hamiltonian  $H_0 = \hat{p}^2/2 + V(x)$  under the momentum space. The maximal band index  $n$  is 51 in our simulations. Electrons near the  $\Gamma$  point ( $k_0 = 0$ ) possess the maximal tunneling probability to be pumped into conduction band, and the holes would be left in the valence band. When one theoretically chooses the initial wave packet constructed by the Bloch states within the range of  $\Delta k$  near the  $\Gamma$  point [35], the initial wave packet approximatively holds a spatially coherent width  $\sigma = \frac{2\pi}{\Delta k}$ .

Then we calculate the laser-induced current  $J(t)$  as the coherent sum of the currents for the different initial states, which is written as

$$J(t) = -\int_{-(\Delta k/2)}^{\Delta k/2} [|\psi_{k_0}(t)\rangle \hat{p} |\psi_{k_0}(t)\rangle] dk_0 + A(t), \quad (2)$$

where the time-dependent wave functions  $|\psi_{k_0}(t)\rangle$  are obtained by the Crank-Nicolson method. The HHG spectra could be obtained as the modulus square of the Fourier transform of the time-dependent current  $J(t)$ . Before the Fourier transform, we multiply  $J(t)$  by a Hanning window to increase the signal-noise ratio.

## B. Quasiparticle picture for multiple Bloch states

Keeping the assumed crystal-momentum range of superposing the initial wave packet in mind, we will reexamine the role of  $\Delta k$  in the process of solid-state HHG. When the laser fields irradiate the wide-band-gap semiconductors, valence-band electrons will be pumped into conduction bands. For the direct band-gap semiconductor the energy gaps become larger toward the boundary of the BZ. Here the frequency of laser fields is lower enough than the minimal gap, the electronic excitation obeys the Landau-Zener-type dependence [36]. Only a small portion of electrons near the minimal band gap can efficiently tunnel to conduction band via the direct interband transition. The valence electrons away from this minimal band gap oscillate back and forth under the drive of laser fields and could further tunnel into the conduction band when they arrive at the minimal band gap. To manipulate experimentally the tunneling-momentum range of electrons, one will beforehand irradiate an appropriate preexcitation pulse [30]. Here the preexcitation photon energy is greater than or equals to the minimal gap. The power and frequency-domain width of the preexcitation pulse could further delicately regulate

the tunneling-momentum range [30,31]. Note that the delayed intense MIR pulse arrives much later than the dephasing time of photon-doping electrons and alone drives coherent HHG. In coordinate space the electronic wave packet (quasiparticle), which is superposed by the involving Bloch states within the crystal-momentum range of  $\Delta k$ , is chosen as the initial wave function in the time-dependent evolution. Taking into account of this assumption, the time-dependent Bloch wave function can be written as  $\psi_k^n(x, t) = e^{i[kx - \epsilon_n(k)t]} u_k^n(x)$ , where  $u_k^n(x)$  is a periodic function. The periodic part  $u_k^n(x)$  of the obtained Bloch wave function involves arbitrary phase, we have performed the phase-correcting scheme [37]. We correct the phase of Bloch wave function by multiplying the term  $e^{-i\theta_i(n)}$ . Here the term  $\theta_i(n)$  is obtained from complex number  $z_{n,i} = |z_{n,i}| e^{i\theta_i(n)} = \int_{\Omega} u_{k_{i+1}}^{n*} u_{k_i}^n d^3x$  in which  $\Omega$  is the volume of the primitive unite cell. The quasiparticle wave-packet  $\Psi_{k_0}^n(x)$  with a central momentum  $k_0 = 0$  in band  $n$  can be superposed from the in-phase Bloch states within the crystal-momentum region  $\Delta k$  [38,39]. It can be denoted as

$$\Psi_{k_0}^n(x, t) = \frac{1}{\Delta k} \int_{-(\Delta k/2)}^{\Delta k/2} \psi_k^n(x, t) dk. \quad (3)$$

Based on the Taylor expansion of eigenenergy  $\epsilon_n(k)$  near  $k_0$  and the assumption that the amplitude modulation factor  $u_k^n(x)$  remains unchanged with  $k$ , Eq. (3) can be rewritten as

$$\Psi_{k_0}^n(x, t) \approx \frac{u_{k_0}^n(x)}{\Delta k} e^{i[k_0x - \epsilon_n(k_0)t]} \times \int_{-(\Delta k/2)}^{\Delta k/2} e^{i\{\delta k[x - \nabla_k \epsilon_n(k)|_{k_0}t]\}} d(\delta k). \quad (4)$$

One finally comes to

$$\Psi_{k_0}^n(x, t) = \psi_{k_0}^n(x, t) \Phi(x, t). \quad (5)$$

It implies that the time-dependent Bloch state  $\psi_{k_0}^n(x, t)$  is modulated by an envelope function  $\Phi(x, t)$ . The envelope function  $\Phi(x, t)$  is defined by [40]

$$\begin{aligned} \Phi(x, t) &= \int_{-(\Delta k/2)}^{\Delta k/2} e^{i\{\delta k[x - \nabla_k \epsilon_n(k)|_{k_0}t]\}} d(\delta k) \\ &\approx \frac{\sin \frac{\Delta k}{2} \zeta}{\frac{\Delta k}{2} \zeta}, \end{aligned} \quad (6)$$

where  $\zeta = x - (\frac{\partial \epsilon_n(k)}{\partial k})_{k_0} t$ . If  $\Delta k$  adopts only the  $\Gamma$  point, the initial wave function is a plane wave with the total delocalization and maximally coherent width  $\sigma$ , i.e., the envelope function  $|\Phi(x, t)| = 1$ . When the initial wave packet is driven by the laser pulses, the momentum range included in the tunneling Bloch electrons determines the wave-particle duality of the time-dependent wave function, which further implies the momentum- or real-space views to understand the HHG process under the picture of electron-hole recombination. The amplitude of the envelope function has a maximum only when the parameter  $\zeta = 0$ . If we define the central position of the time-dependent wave packet as the coordinate of the initial wave packet, it can be written as

$$x = \left( \frac{\partial \epsilon_n(k)}{\partial k} \right)_{k_0} t. \quad (7)$$

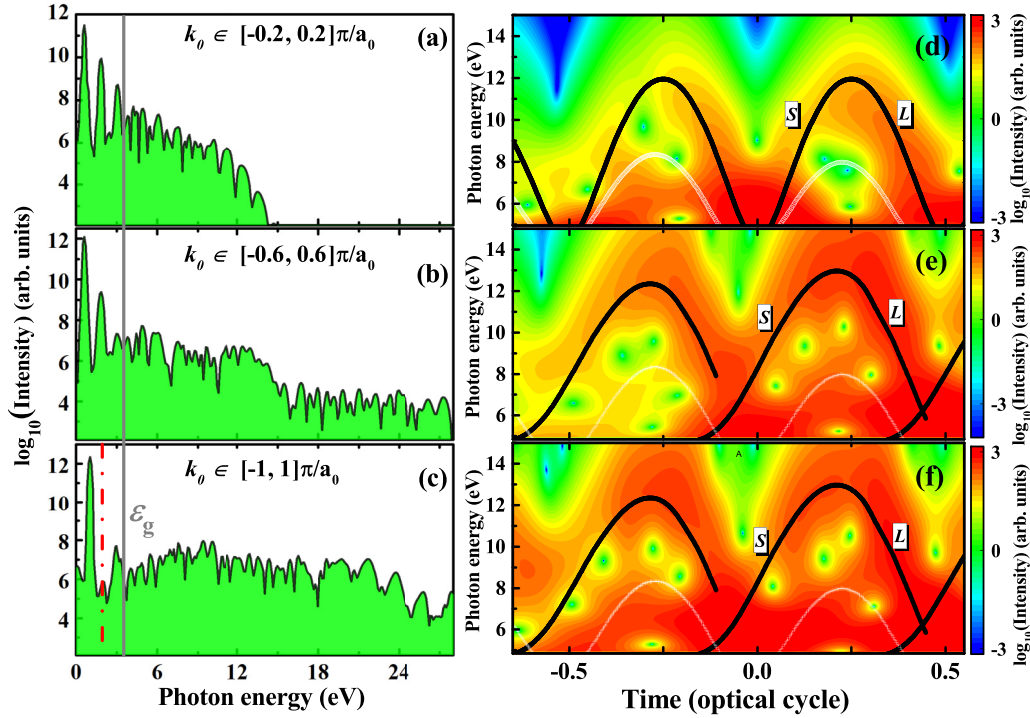


FIG. 1. Effect of the tunneling-momentum range  $\Delta k$  in the HHG spectra. (a)–(c) present the HHG spectra in which the tunneling-momentum ranges  $\Delta k$  are  $0.4\pi/a_0$ ,  $1.2\pi/a_0$ , and  $2\pi/a_0$ , respectively. The color maps of (d)–(f), respectively, show the time-frequency profiles in the HHG spectra (a)–(c). In (a)–(c), the vertical gray line marks the minimal energy gap  $\epsilon_g$ , and the spectroscopic dip is specified by the red dash-dot line. In (d)–(f), the black and white thick curves, respectively, denote the first and second recombination times obtained from classical predictions. The symbols  $S$  and  $L$ , respectively, denote the short and long trajectories in the first-recollision process.

The group velocity of the wave packet in the real space can be written as

$$v_n^g(k) = \dot{x} = \left. \frac{\partial \epsilon_n(k)}{\partial k} \right|_k. \quad (8)$$

Under the drive of the laser fields, the electron and hole wave packets propagate with their respective group velocities  $v_n^g$  ( $n = e, h$ ). The high harmonics with band-gap energy would be emitted when the excited electron and corresponding hole recombine with each other in real space. Here, the relative displacement between electron and hole is denoted as

$$\Delta x = x_e - x_h = \int_{t'}^t v_e^g[k(\tau)]d\tau - \int_{t'}^t v_h^g[k(\tau)]d\tau, \quad (9)$$

where  $x_e$  ( $x_h$ ) represents the displacement of electrons (holes) from ionization moment  $t'$  to recombination moment  $t$ . The condition of HHG emission satisfies the zero displacement in the recombination step [32], i.e., the so-called closed-trajectory model applied in Figs. 1(e) and 1(f). However, in the open-trajectory model the relative displacement  $\Delta x$  is nonzero [23,41]. This nonzero overlap between electron and hole wave packets is related to the coherent width  $\sigma$  and applies to Fig. 1(d) with a coherent width  $4a_0$ .

### III. RESULTS AND DISCUSSIONS

#### A. Temporal and spectral HHG characteristics

In Figs. 1(a)–1(c) we first make a comparison between HHG spectra via choosing different tunneling-momentum

regions. The characteristic variations in the HHG spectra with the increasing region of the initial momenta could be enumerated as follows: (i) the extension of the cutoff frequency; (ii) the spectroscopic dip appearing in the below-gap harmonics.

Considering the fact that the valence electrons away from the minimal gap can tunnel directly into the lowest conduction band and more easily be pumped into the high-lying conduction band via the help of a minimum band gap between two conduction bands at the edge of the BZ; the extension of the cutoff frequency with the growing tunneling-momentum region has been clarified. Thus, the broader region of  $\Delta k$  leads to the emergence of the second HHG plateau in Fig. 1(b) and can further merge the two HHG plateaus in Fig. 1(c). To distinguish the temporal characteristic of the harmonic emissions in Figs. 1(a)–1(c) and make an assessment on the wave-particle duality of the time-dependent Bloch wave packet, we show their time-frequency profiles in Figs. 1(d)–1(f), respectively [42]. In addition, we also extract the the first- and secondary-recollision times based on the quasiclassical trajectory predictions in Eq. (9) as depicted by black and white curves, respectively, in Figs. 1(d)–1(f). One could observe that their emission times in the quantum simulations reach a great agreement with the first- and secondary-recollision times obtained from the open- or closed-trajectory models. However, the temporal characteristic of the first-recollision times in Fig. 1(d) is different from that in Figs. 1(e) and 1(f) as shown by the black curves. In Fig. 1(d) the temporal durations for the short and long trajectories are equal and about 0.25 optical cycle. However, this situation changes for the short- and long-trajectory durations in Figs. 1(e) and 1(f) in which

the short- and long-trajectory durations are about 0.4 and 0.25 optical cycles, respectively. Note that the short-trajectory duration gradually increases with the growing region of  $\Delta k$ . In retrospect, in atomic and molecular HHGs the duration of the short trajectory is longer than that of the long trajectory (i.e., the closed-trajectory characteristic) due to the fact that their localized electronic wave packets can be regarded as a classical particle. Figures 1(e) and 1(f) showing the closed-trajectory characteristic imply that the time-dependent wave packet depicted by Eq. (3) with a broader range of  $\Delta k$  is spatially localized and similar to the situation in atomic and molecular systems. In contrast, in Fig. 1(d) its time-dependent wave packet involves a narrower  $\Delta k$  in Eq. (3) and, thus, shows the spatial delocalization (or larger coherent width  $\sigma$ ) in which the high-harmonic emissions follow the open-trajectory temporal characteristic. Comparing with Fig. 1(d), in addition, one can further confirm a secondary-recollision process via excluding the contribution from the interband transitions between high-lying conduction bands (continued states) reported previously [14] as shown by the white curves in Figs. 1(e) and 1(f). The secondary-recollision trajectories of the electronic wave packet further reflect its quality of the particle.

### B. Modulation of HHG yields

Before we explain the spectroscopic dip within the below-gap harmonics shown in Fig. 1(c), we first illustrate the HHG yields with the increasing  $\Delta k$ . The HHG yield for below-gap harmonics ( $Y_{\text{below}}$ ) is calculated by integrating the range of photon energy from 0 to 4.2 eV, whereas the yields for plateau zone ( $Y_{\text{plateau}}$ ) is integrated within the spectroscopic range of 4.2–12 eV. In Fig. 2(a), one can see that  $Y_{\text{below}}$  (violet dash-dot line) increases slightly, reaches its maximum at about  $\Delta k = 0.13\pi/a_0$  and rapidly decays with the further growing of  $\Delta k$ . For  $Y_{\text{plateau}}$  shown by the violet solid line in Fig. 2(a), some delicate modulations appear in the mainly decreased tendency. To reveal the tendencies in  $Y_{\text{below}}$  and  $Y_{\text{plateau}}$ , we present the electronic population ( $\rho_c$ ) of pumping into conduction bands at the end of laser fields as denoted by green solid dots in Fig. 2(a). The electronic population  $\rho_c$  increases first, reaches the maximal value near  $\Delta k = 0.5\pi/a_0$ , and decreases soon with the increase in  $\Delta k$ . Thus, the slight increase in  $Y_{\text{below}}$  at small  $\Delta k$  and some subtle modulations in  $Y_{\text{below}}$  and  $Y_{\text{plateau}}$  can be qualitatively comprehended by the variation in the electronic population  $\rho_c$ . Note that the differences between electronic population  $\rho_c$  and HHG yields imply the role of intraband transport in solid-state HHG and will be discussed later.

In the above, we discuss the overall trend of HHG yields. According to the separation of intra- and interband contributions under the picture of the Houston basis [35], in Fig. 2(b) we then show the ratio between intra- and interband harmonic yields as a function of  $\Delta k$ . As reported in previous works, the below-gap and plateau-zone harmonics were dominated by the intra- and interband emissions, respectively [6,11,13]. For a given range  $\Delta k$ , the yield ratio between the intra- and interband contributions is denoted as  $\eta_s = Y_s^{\text{intra}}/Y_s^{\text{inter}}$  in which  $s \equiv \text{below}$ . The yield ratios within the below-gap region are denoted as  $\eta_{\text{below}}$ . In Fig. 2(b) one can clearly see that  $\eta_{\text{below}}$

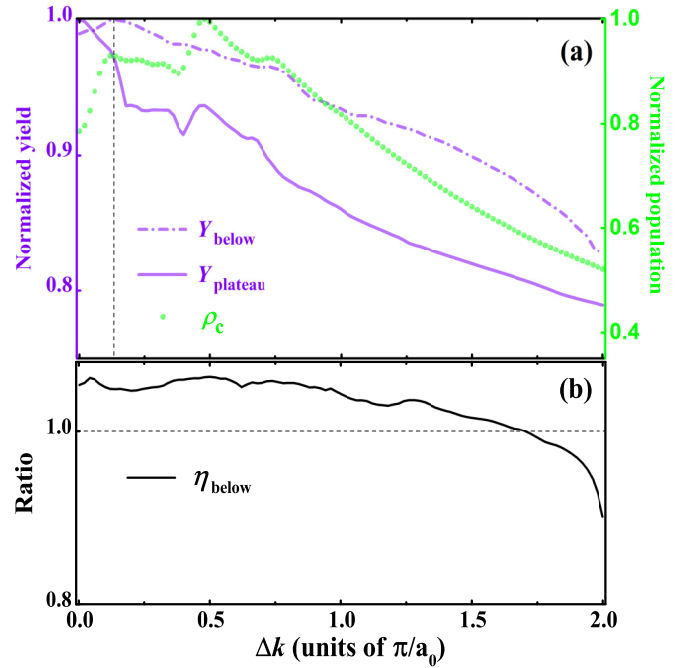


FIG. 2. (a) The below-gap ( $Y_{\text{below}}$ ) and plateau-zone ( $Y_{\text{plateau}}$ ) yields as a function of  $\Delta k$ .  $\rho_c$  is the electronic population of pumping into conduction bands at the end of laser pulses. (b) Yield ration ( $\eta$ ) between intra- and interband emissions as a function of  $\Delta k$ . The black solid curve denotes the results for the below-gap zone.

decreases gradually with the increasing  $\Delta k$ . Similarly, there is some subtle modulations in the ratios. When  $\Delta k$  is greater than  $1.7\pi/a_0$ , the ratio  $\eta_{\text{below}}$  will be less than 1.0, which reflects that the interband current dominates the below-gap HHG emissions, and is contrary to previous reports [11,13]. The yields of below-gap harmonics dominated by the interband process will decay with an extreme rate when the order is increasing, which leads to the emergence of spectroscopic dip shown in Fig. 1(c). Actually, for the photocarrier-doping ZnO crystal driven by midinfrared laser fields, the phenomenon that the below-gap emission is dominated by the interband current had been observed experimentally under the situation of suppressing extremely the intraband current [30]. Its mechanism was not carefully discussed.

Hereafter, we highlight the role of carrier distribution, resulting with the intraband transport, in solid-state HHG. To unravel the impact of intraband transport, the intraband current under the Houston basis can be written as [35]

$$\begin{aligned}
 J_{\text{intra}}(t) &= \sum_{n=e,h} \int_{-(\Delta k/2)}^{\Delta k/2} \langle \psi_{nk_0(t)} | \hat{p} | \psi_{nk_0(t)} \rangle dk_0 \\
 &= \sum_{n=e,h} \int_{-(\Delta k/2)}^{\Delta k/2} v_n^s[k_0(t)] |\psi_{nk_0(t)}|^2 dk_0. \quad (10)
 \end{aligned}$$

Here  $k_0(t) \equiv k_0 - A(t)$  and  $|\psi_{nk_0(t)}|^2$  denote the time-dependent electron or hole populations possessing the  $k$  resolution within the energy band. In the BZ, the electron and hole group velocities satisfy the odd symmetry  $v_n^s(-k) = -v_n^s(k)$ .



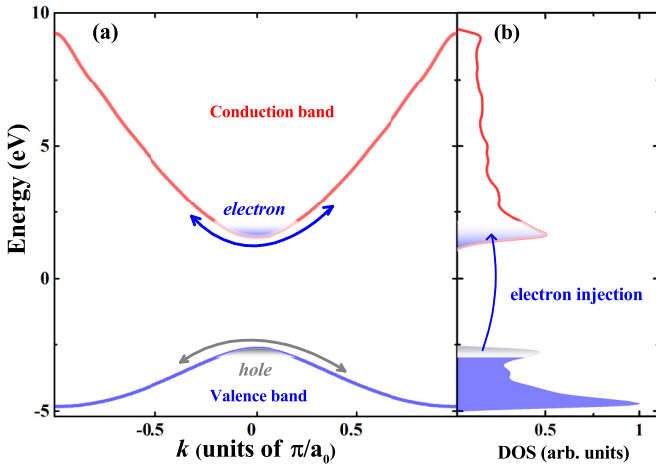


FIG. 3. Schematic of the starting intraband transport of carrier within energy bands. (a) The electrons pumped into the conduction band and the remaining holes in the valence band start to transport in their respective energy bands under the drive of laser fields. The two double-headed-arrow curves in (a) denote the subsequent drive of laser pulses on the electrons and holes. (b) The density of states and the initial carrier (electron and hole) distributions in the valence and conduction bands. In (b), the vertically single-headed-arrow curve represents the electronic pump induced by the irradiation of the preexcitation pulse.

In Fig. 3(a), we show the schematic describing the initial distributions of the preexcited electrons and holes within their respective energy bands. Here the situation of carrier distribution could be controlled experimentally via the photon-carrier doping as mentioned above. Taking the case of the tunneling-momentum region  $\Delta k = 0.4\pi/a_0$  as example, the electrons are pumped into the conduction band and their counterpart holes remain in the valence band. One sees that the  $k$ -resolution distributions for the electron and hole are symmetrical around the  $\Gamma$  point. Considering the initial distributions of the carrier and their energy-dependent DOS shown in Fig. 3(b), their symmetrical distribution in the BZ could be destroyed naturally by the subsequent drive of the MIR laser pulses, which results in the intraband current. Keeping the odd symmetry of the group velocity of Eq. (10) in mind, the fully occupied valence band or the totally unoccupied conduction band will not contribute to the intra- and interband currents. Thus, the degree of breaking the symmetrical distribution will vary with the initially occupied range of carriers in the BZ.

To assess the time-dependent symmetrical distribution of carrier within the respective energy bands, in Fig. 4 we take the electron as an example and show the time-dependent electronic populations within the conduction band under the two cases of tunneling-momentum region  $\Delta k$ . For the case with a narrow tunneling-momentum region, the time-dependent electronic distribution shown in Fig. 4(a) almost follows the oscillation of the laser vector potential and displays the extremely asymmetrical distribution regarding to the center  $\Gamma$  point, which gives rise to the maximal current. However, in Fig. 4(b) with a broadest tunneling-momentum region, the time-dependent electronic distribution in the BZ becomes relatively symmetrical regarding the  $\Gamma$  point and, thus, con-

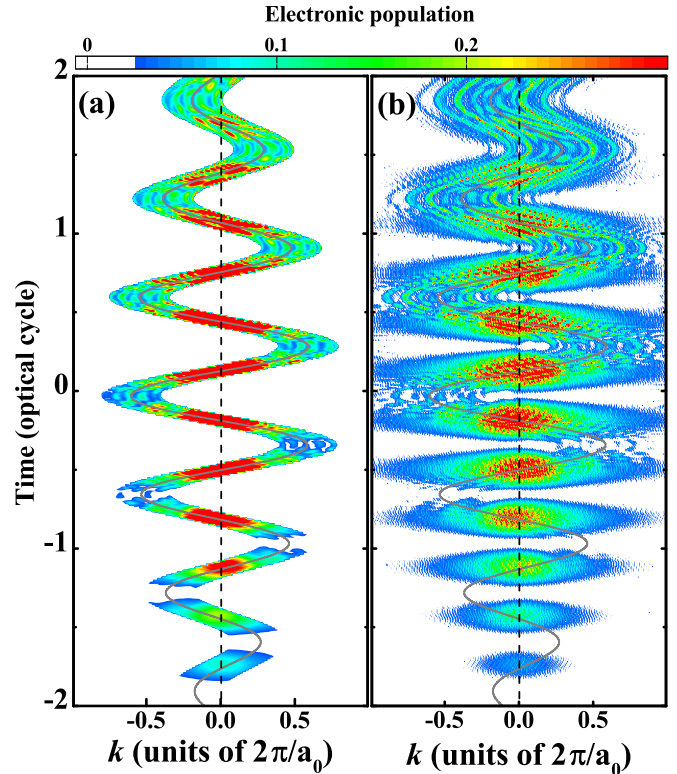


FIG. 4. The time-dependent conduction-band population for the cases with the initial tunneling-momentum regions  $0.4\pi/a_0$  in (a) and  $2\pi/a_0$  in (b). The oscillating curves in (a) and (b) are the vector potentials of the laser fields. The vertical dashed lines mark the  $\Gamma$  point in the BZ.

tributes to a weaker current. In fact, the distribution of carrier gradually gets symmetrical with the growing tunneling-momentum region, which leads to the fact that the total current in solids induced by the drive of MIR laser fields will become weaker. Thus, the general damping tendency of HHG yield and electronic population shown in Fig. 2(a) have been revealed successfully.

In addition, the suppressed electronic populations around the peaks of the electric field (zeros of the laser vector potential) and the fine fingerprints of electronic population can be observed in Fig. 4(b) comparing with Fig. 4(a). These features of electronic population in Fig. 4(b) manifest the quantum interference between different initial  $k_0$  electrons. Let us make an estimation of the interference-free range of momentum as shown in Fig. 4(a). Within the tunneling-momentum region  $\Delta k$ , the interference condition is governed by

$$\Delta\phi = \int_0^{\Delta k/F_0} \{\epsilon_e[k_0(t')] - \epsilon_h[k_0(t')]\} dt', \quad (11)$$

where  $\Delta k/F_0$  is the propagating time delay between the electrons within this  $\Delta k$ , and  $F_0$  is the amplitude of the electric field. For the small region  $0.13\pi/a_0$  marked by the vertical dashed lines in Fig. 2(a), the maximal dynamical phase difference is approximately equal to  $0.3\pi$ , which leads to the increase in electronic population  $\rho_c$  within this small momentum region as shown by green solid dots in Fig. 2(a). Considering the growing tunneling-momentum region

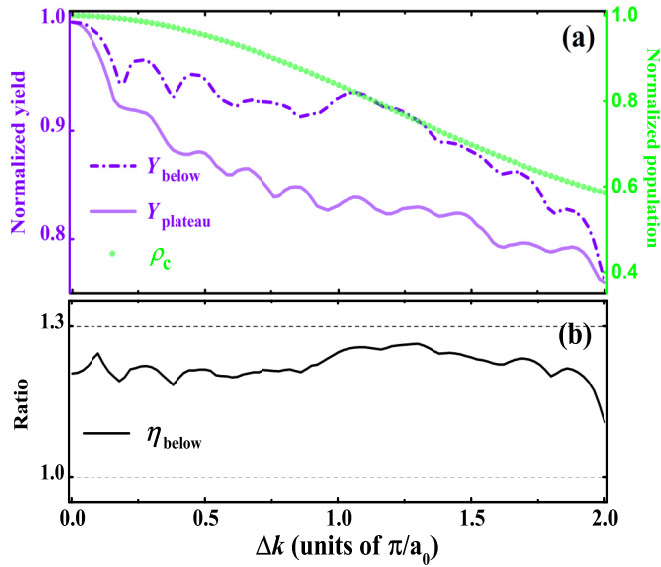


FIG. 5. Role of dephasing time in HHG with the increasing tunneling-momentum region. The dephasing time adopted here is a quarter of optical cycle. The caption of curves is same as Fig. 2.

resulting in a longer propagating time delay, the subtle modulations in  $Y_{\text{below}}$  and  $Y_{\text{plateau}}$  as shown in Fig. 2(a), can partly attribute to the complex intra- and intercycle interference between electrons excited around various peaks of the laser pulse. These schemes of quantum interference had been discussed carefully in Refs. [43–45].

### C. Role of dephasing in HHG spectra

Finally, we discuss the role of dephasing time in HHG with the increasing tunneling-momentum region. As reported in Ref. [23], a shorter dephasing time will highlight the particle nature of the time-dependent wave packet. Furthermore, the dephasing process gradually destroys the intra- and intercycle interference but survives the interference between the electrons within their tunneling-momentum regions  $\Delta k$ . As shown in Fig. 5(a), the regularly modulated HHG yields and the monotonously decayed  $\rho_c$  verify our claims. One can

further observe that the crystal-momentum interval between two adjacent minima in the oscillated HHG yields is approximate to  $0.2\pi/a_0$ . Because of the linearly growing band gap toward the edge of the BZ and the growing propagating time delay, this crystal-momentum interval nicely corresponds to the increase indynamical phase difference  $\Delta\phi = 2\pi$  obtained from Eq. (11). In addition, the situation that the interband contribution dominates the below-gap harmonic disappears in Fig. 5(b) when the dephasing is switched on. At the same time, the spectroscopic dip vanishes from the below-gap harmonics. Thus, one can understand the failure to observe the spectroscopic dip in experiments.

## IV. CONCLUSION

To conclude, we study the temporal characteristic of the high-harmonic emissions when the involving crystal-momentum region is increasing. To unravel the electron and hole dynamics in solids driven by the external field, a quasiparticle picture of the Bloch wave-packet motion has been introduced in which the quasiparticle is obtained from the superposition of the Bloch states within the involving crystal-momentum region. The crystal-momentum region of generating the electron-hole pair determines the spatially localized feature of the electron-hole wave packet, and the coherent overlap between electron and hole wave packets dominates the temporal characteristics of high-harmonic emissions. Finally, we unravel the physical origin in the attenuation of HHG yield with the growing tunneling-momentum region, which is attributed to the gradual symmetry of time-dependent carrier population regarding the  $\Gamma$  point. Experimentally, the photon-carrier doping is a feasible scheme by manipulating the preexcitation pulse. Our results provide a way to regulate the temporal emission of HHG and the photon-induced current in solids.

## ACKNOWLEDGMENT

This work was supported by the National Natural Science Foundation of China (NSFC) (Grant No. 11904331).

- 
- [1] F. Krausz and M. Ivanov, *Rev. Mod. Phys.* **81**, 163 (2009).
  - [2] S. Y. Kruchinin, F. Krausz, and V. S. Yakovlev, *Rev. Mod. Phys.* **90**, 021002 (2018).
  - [3] K. A. Pronin and A. D. Bandrauk, *Phys. Rev. Lett.* **97**, 020602 (2006).
  - [4] Ó. Zurrón-Cifuentes, R. Boyero-García, C. Hernández-García, A. Picón, and L. Plaja, *Opt. Express* **27**, 7776 (2019).
  - [5] S. Ghimire, A. D. DiChiara, E. Sistrunk, P. Agostini, L. F. DiMauro, and D. A. Reis, *Nat. Phys.* **7**, 138 (2011).
  - [6] G. Vampa, T. J. Hammond, N. Thiré, B. E. Schmidt, F. Légaré, C. R. McDonald, T. Brabec, and P. B. Corkum, *Nature (London)* **522**, 462 (2015).
  - [7] T. T. Luu, M. Garg, S. Yu. Kruchinin, A. Moulet, M. T. Hassan, and E. Goulielmakis, *Nature (London)* **521**, 498 (2015).
  - [8] B. Zaks, R. B. Liu, and M. S. Sherwin, *Nature (London)* **483**, 580 (2012).
  - [9] F. Langer, M. Hohenleutner, C. Schmid *et al.*, *Nature (London)* **533**, 225 (2016).
  - [10] G. Ndashimiye, S. Ghimire, M. Wu *et al.*, *Nature (London)* **534**, 520 (2016).
  - [11] G. Vampa, C. R. McDonald, G. Orlando, D. D. Klug, P. B. Corkum, and T. Brabec, *Phys. Rev. Lett.* **113**, 073901 (2014).
  - [12] T.-Y. Du, *Phys. Rev. A* **100**, 053401 (2019).
  - [13] G. Vampa, C. R. McDonald, G. Orlando, P. B. Corkum, and T. Brabec, *Phys. Rev. B* **91**, 064302 (2015).
  - [14] T.-Y. Du and X.-B. Bian, *Opt. Express* **25**, 151 (2017).
  - [15] K. K. Hansen, T. Deffge, and D. Bauer, *Phys. Rev. A* **96**, 053418 (2017).

- [16] P. G. Hawkins, M. Y. Ivanov, and V. S. Yakovlev, *Phys. Rev. A* **91**, 013405 (2015).
- [17] T.-Y. Du, *Opt. Lett.* **46**, 2007 (2021).
- [18] M. Holthaus, *Phys. Rev. Lett.* **69**, 351 (1992).
- [19] F. H. M. Faisal and J. Z. Kamiński, *Phys. Rev. A* **54**, R1769 (1996).
- [20] F. H. M. Faisal and J. Z. Kamiński, *Phys. Rev. A* **56**, 748 (1997).
- [21] D. Dimitrovski, T. G. Pedersen, and L. B. Madsen, *Phys. Rev. A* **95**, 063420 (2017).
- [22] T. N. Ikeda, K. Chinzei, and H. Tsunetsugu, *Phys. Rev. A* **98**, 063426 (2018).
- [23] G. Wang and T.-Y. Du, *Phys. Rev. A* **103**, 063109 (2021).
- [24] C. Yu, K. K. Hansen, and L. B. Madsen, *Phys. Rev. A* **99**, 063408 (2019).
- [25] C. Yu, K. K. Hansen, and L. B. Madsen, *Phys. Rev. A* **99**, 013435 (2019).
- [26] N. Tancogne-Dejean, O. D. Mücke, F. X. Kärtner, and A. Rubio, *Phys. Rev. Lett.* **118**, 087403 (2017).
- [27] F. Navarrete, M. F. Ciappina, and U. Thumm, *Phys. Rev. A* **100**, 033405 (2019).
- [28] K. K. Hansen, D. Bauer, and L. B. Madsen, *Phys. Rev. A* **97**, 043424 (2018).
- [29] L. Yue and M. B. Gaarde, *Phys. Rev. A* **103**, 063105 (2021).
- [30] Z. Wang, H. Park, Y. H. Lai *et al.*, *Nat. Commun.* **8**, 1686 (2017).
- [31] C. Heide, Y. Kobayashi, A. Johnson, F. Liu, T. F. Heinz, D. A. Reis, and S. Ghimire, [arXiv:2109.04508](https://arxiv.org/abs/2109.04508).
- [32] P. B. Corkum, *Phys. Rev. Lett.* **71**, 1994 (1993).
- [33] M. Lewenstein, P. Balcou, M. Y. Ivanov, A. L'Huillier, and P. B. Corkum, *Phys. Rev. A* **49**, 2117 (1994).
- [34] J. C. Slater, *Phys. Rev.* **87**, 807 (1952).
- [35] M. Wu, S. Ghimire, D. A. Reis, K. J. Schafer, and M. B. Gaarde, *Phys. Rev. A* **91**, 043839 (2015).
- [36] H. Taya, M. Hongo, and T. N. Ikeda, *Phys. Rev. B* **104**, L140305 (2021).
- [37] U. Lindelfelt, H.-E. Nilsson, and M. Hjelm, *Semicond. Sci. Technol.* **19**, 1061 (2004).
- [38] K. Huang, *Solid State Physics* (Higher Education Press, Beijing, China, 1988).
- [39] J. M. Ziman, *Principles of the Theory of Solids* (Cambridge University Press, Cambridge, U.K., 1972).
- [40] T.-Y. Du, X.-H. Huang, and X.-B. Bian, *Phys. Rev. A* **97**, 013403 (2018).
- [41] J. A. Crosse and R.-B. Liu, *Phys. Rev. B* **89**, 121202(R) (2014).
- [42] C. Chandre, S. Wiggins, and T. Uzer, *Physica D* **181**, 171 (2003).
- [43] T.-Y. Du, D. Tang, and X.-B. Bian, *Phys. Rev. A* **98**, 063416 (2018).
- [44] J.-Z. Jin, X.-R. Xiao, H. Liang, M.-X. Wang, S.-G. Chen, Q. Gong, and L.-Y. Peng, *Phys. Rev. A* **97**, 043420 (2018).
- [45] T.-Y. Du and S.-J. Ding, *Phys. Rev. A* **99**, 033406 (2019).